Preliminary model of the plasma expansion in a magnetic arch thruster (and overview of the first prototype)

IEPC-2022-423

Presented at the 37th International Electric Propulsion Conference
Massachusetts Institute of Technology, Cambridge, MA, USA
June 19-23, 2022

Mario Merino[1], Diego García-Lahuerta, Célian Boyé, Jaume Navarro-Cavallé, Eduardo Ahedo
Equipo de Propulsión Espacial y Plasmas (EP2), Universidad Carlos III de Madrid, Leganés, Spain

The novel magnetic arch thruster concept is presented, which features a 'C'-shaped discharge chamber and a toroidal applied magnetic field. A preliminary collisionless, quasineutral, two-fluid model of the external plasma expansion beyond the two outlets of the thruster, into what is termed the magnetic arch, is introduced. Planar 2D geometry and the $\beta = 0$ limit are assumed to simplify this first version of the model. The plasma properties (density, electron temperature, electrostatic potential, ion velocity, out-of-plane currents) are analyzed, and the magnetic thrust density discussed. It is shown that the ions form a beam that propagates beyond the closed lines of the applied magnetic field, albeit at the price of a small contribution of magnetic drag in the latter part of the expansion. A preliminary study of the plasma-induced magnetic fields is included and it is hypothesized that the topology change caused by it in the total field can improve this situation. The limitations of the present model are indicated. As a bonus, we also overview of the first prototype of the magnetic arch thruster.

I. Introduction

Magnetically-guided plasma expansions are a central part of the operation of electrodeless plasma thrusters (EPTs) [1–4]. Traditionally, EPTs use an axisymmetric magnetic nozzle (MN) to externally expand and accelerate the plasma generated by the source [5–9]. This is the case of e.g. the helicon plasma thruster (HPT) [10–16] and the electron-cyclotron plasma thruster (ECRT) [17–20]. Additionally, non-axisymmetric MNs have been proposed for contactless thrust vector control [21].

MNs work by radially confining the expansion of the warm plasma electrons, which must be well magnetized. This confinement occurs thanks to the diamagnetic azimuthal electron current density $j_{\theta e} = -enu_{\theta e}$ that form as a consequence of the existence of a perpendicular electron pressure gradient and the $\boldsymbol{E} \times \boldsymbol{B}$ drift. This current density give rise to a magnetic force density in the plasma. Part of this force density is confining/radial ($j_{\theta e} B_z$), while the other part is accelerating/axial ($-j_{\theta e} B_r$). As a reaction, the induced magnetic field created by this current density exerts a force on the thruster magnetic circuit, which is known as magnetic thrust. The parallel force on the electrons is balanced by the self-consistent axial ambipolar electrostatic field that forms in the MN. This field confines electrons and accelerates ions, converting the electron thermal energy into directed kinetic ion energy. Downstream, the plasma jet must eventually separate from the returning magnetic lines to prevent the increase of plume divergence and the cancellation of thrust [6]. It should be noted that, at least for hot-electron and cold-ion plasmas, ions do not need to be magnetized for the MN to operate as intended; indeed, a high ion magnetization is generally undersirable, as it makes plasma detachment occur farther downstream, and promotes the appearance of a paramagnetic azimuthal ion current density $j_{\theta i} = enu_{\theta i}$ in the plasma that results in magnetic drag [5]. However, special devices, such as the variable specific impulse magnetoplasma rocket (VASIMR) [22], rely on the expansion of hot ions, where ion magnetization could be a necessity.

Existing EPTs have a cylindrical discharge chamber, and the MN opens at one end of it. The other end is a dielectric wall upon which magnetic lines impinge essentially perpendicularly, and large plasma losses are attributed to this region due to the lack of magnetic confinement.

---

[1] mario.merino@uc3m.es

In the novel magnetic arch thruster (MAT) EPT concept, the cylindrical plasma source is replaced by a "C"-shaped chamber, enveloped by coils that create a magnetic field essentially parallel to the walls. By removing the rear wall and ensuring full magnetic shielding of the remaining walls, it is hypothesized that this geometry could bring advantages with regards to losses. In order to proof or disproof this hypothesis, a numerical and experimental research effort is being undertaken as part of the ERC Starting Grant ZARATHUSTRA project, which aims to unravel the physical underpinnings of electrodeless plasma thrusters and revolutionize their design.

As a result of the MAT configuration, the magnetic field outside of the device has a different topology: the external field of the MAT consists of two MNs of opposite polarity, whose magnetic lines connect downstream, creating a closed-line configuration, which we have termed magnetic arch (see figure 1). While intrinsic to the MAT, this external geometry is also relevant for clusters of cylindrical EPTs, where polarities should be alternated to minimize plume divergence, forming similar magnetic setups, and therefore worth studying on its own.

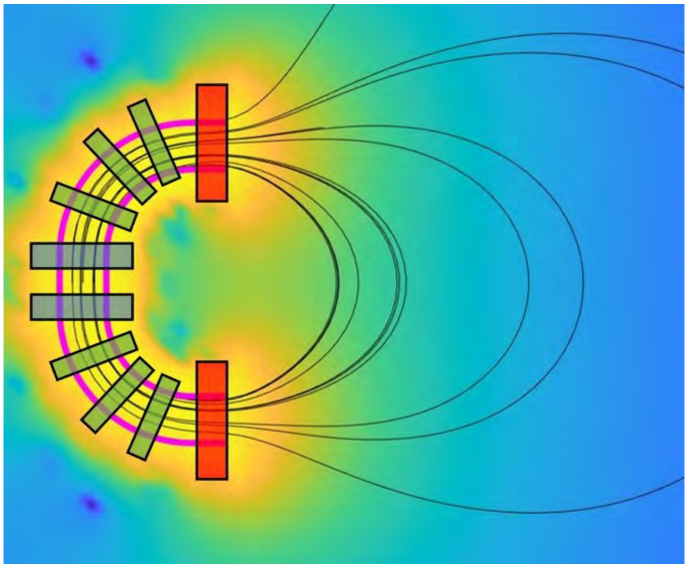

Fig. 1 Example geometry of a magnetic arch thruster (MAT). The "C"-shaped ionization chamber (pink), the magnetic coils (colored boxes), and some magnetic lines (black) are shown.

A major difference between an axisymmetric MN and the magnetic arch of the MAT is that, while in a single MN the plasma flux is roughly parallel to the applied field $\boldsymbol{B}_a$ everywhere, in a magnetic arch the flux is only parallel initially; downstream, where the lines of the two MNs connect, the plasma flux must necessarily traverse the applied field roughly perpendicularly. Also, while in the MN the plasma currents are predominantly diamagnetic (i.e., thrust producing), in the MAT plasma expansion, the paramagnetic currents are necessarily large in this connection region. Relatedly, while in a MN the plasma-induced magnetic field $\boldsymbol{B}_p$ plays a secondary role in deforming the shape of the lines, increasing divergence minimally if the MN is well-designed [23], and can be ignored in first studies, it is expected to play a central role in the MAT, stretching the closed-line topology and changing it into a completely different topology. Finally, the interaction of the two plasma jets coming from each end of the device may lead to shock-like structures in the plume, not found in smooth MN plasma expansions [5]. Altogether, it is anticipated that the topology of the magnetic arch should lead to a plasma plume featuring a smaller divergence angle than a comparable MN. The existence of two separate device exits also opens the way to enhanced magnetic thrust vector control, in ways not possible with a single MN.

This contribution is a first effort toward the modeling the MAT plasma expansion. The goal is to set up a simple yet meaningful theoretical framework from which it is possible to understand the fundamental mechanisms at play, and which can be extended in the future to include more advanced phenomena. A first steady-state plasma expansion is studied, discussing in particular magnetic thrust production. Finally, we identify the main physics currently outside of the model that must be taken into account in future iterations. However, the major limitations of the study can be already stated from the outset: firstly, we only study a 2D planar development of the MAT, rather than the ful 3D geometry. Secondly, we ignore plasma kinetics, and employ a collisionless multi-fluid plasma model. Thirdly, and crucially, we ignore for now the plasma-induced magnetic field in the solution of the plasma flow by taking the $\beta = 0$ limit, although we estimate it a posteriori (i.e., non self-consistently) to discuss its central importance.

In a parallel effort, a first prototype of the MAT is being built, with the purpose of experimentally validating the concept and enabling the comparison with simulations. A brief description of the prototype is included in this contribution.

The rest of the document is structured as follows. Section II presents the mathematical model of the MAT and describe the approach followed to integrate it numerically. Section III contains the results of the first MAT simulation using this model, including plasma density, ion velocity, electrostatic potential, plasma currents, and magnetic thrust. Section IV then discusses the plasma-induced magnetic field that can be estimated from this first plasma solution, and how its presence is expected to drastically change the results with respect to the $\beta = 0$ case. Section V introduces the experimental prototype of the MAT being developed. Finally, section VI briefly gathers the main points of this work and defines the next steps in this research effort.

II. Model

The preliminary MAT model is a two-dimensional, two-fluid (ions and electrons) model of the steady-state plasma flow in a given applied magnetic field $\boldsymbol{B}_a$. The model takes the following assumptions:

1) Quasineutral, collisionless, fully-ionized plasma.
2) Inertialess, Maxwellian, perfectly-magnetized electrons with a polytropic exponent γ.
3) Cold, singly-charged ions, with arbitrary magnetization, emitted from each source exit. Moreover, ions are assumed to remain cold downstream, neglecting the effects of any shock wave-like discontinuities on ion temperature that may exist in the solution.
4) Planar-symmetric geometry, as an intermediate step toward the actual three-dimensional geometry of the device. We consider the meridian plane of the plume and assume an infinite plasma with uniform properties in the perpendicular direction.

The total magnetic field is $\boldsymbol{B} = \boldsymbol{B}_a + \boldsymbol{B}_p$. However, in this first model the $\beta = \mu_0 n T_e / B_a^2 = 0$ limit is assumed, so $\boldsymbol{B} = \boldsymbol{B}_a$. The plasma-induced field $\boldsymbol{B}_p$, assumed zero for now, will be estimated a posteriori from the resulting plasma currents for cases with $\beta \neq 0$. Finally, the approach used to reach steady state will be a near-physical time evolution from an initial condition, where some of the temporal terms may be neglected to simplify the equations.

To normalize the model, we select m_i, e, and a length R (e.g. radius of one of the plasma thruster exits). And, using the properties at the center point of one of the two symmetric outlets (where variables are marked with subindex 0), the electron temperature T_{e0} (in energy units) and the ion density n_0 used for injection. Note that, even if flux coming from one outlet ever arrives at the other, T_{e0} and n_0 are defined from the single-beamlet properties. This center point is also chosen as the origin of the electrostatic potential, so $\phi_0 = 0$ there. In the following, all symbols are already appropriately dimensionless. In particular, the value of the magnetic field B at the center of the outlet, B_{a0}, coincides numerically with the dimensionless ion gyrofrequency Ω_{i0}, and defines the (initial) ion magnetization degree.

Sketch 2 depicts the problem domain We define a right-handed reference frame with origin O on the exit plane of the plasma source, Oz axis pointing downstream. The "C" shaped centerline of the thruster is contained in the Oxz plane, which is the plane under study. The Oy axis is perpendicular to it, and in this direction we preliminarly model the plasma as infinite and uniform. The plane Oyz is a symmetry plane, and only the upper half of the plane ($x \geq 0$) will be simulated, as shown in the figure.

We introduce the Cartesian vector basis $\{\mathbf{1}_x, \mathbf{1}_y, \mathbf{1}_z\}$. We also define $\mathbf{1}_b = \boldsymbol{B}/B$ and $\mathbf{1}_\perp = \mathbf{1}_y \times \mathbf{1}_b$, and define the magnetic vector basis $\{\mathbf{1}_b, \mathbf{1}_\perp, \mathbf{1}_y\}$. Both bases are right-handed and orthonormal.

The planar magnetic field accepts the magnetic streamfunction $\psi_B(z,x) = \psi_{Ba}(z,x)$, satisfying:

$$\frac{\partial \psi_B}{\partial z} = -B_x, \qquad \frac{\partial \psi_B}{\partial x} = B_z. \tag{1}$$

Magnetic lines are labeled by ψ_B. Under the assumption of full electron magnetization, electron streamlines coincide with magnetic lines; however, ion streamlines may differ from magnetic lines, however. Note that:

$$\mathbf{1}_\perp = \nabla \psi_B / B; \qquad \text{and:} \qquad \nabla f = \frac{\partial f}{\partial \mathbf{1}_\perp} \mathbf{1}_\perp = B \frac{\mathrm{d} f(\psi_B)}{\mathrm{d}\psi_B} \mathbf{1}_\perp \tag{2}$$

for any single-variable function $f(\psi_B)$.

The magnetic field $\boldsymbol{B}_a$ is generated by the linear superposition of four ideal thin wires in the $\mathbf{1}_y$ direction, located on the $z = 0$ plane. The magnetic field strength and streamfunction of a single wire carrying a electric current I can be

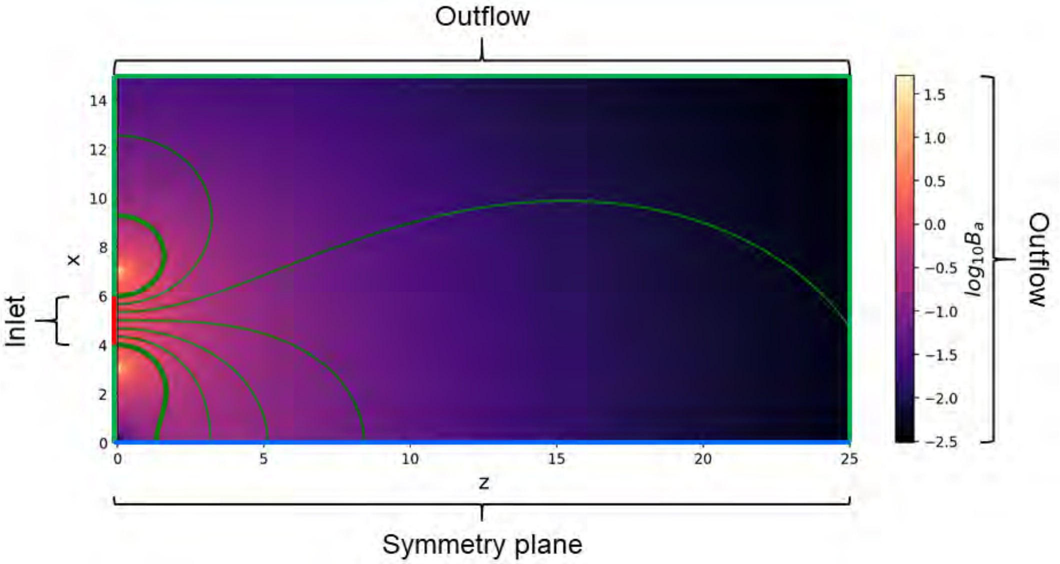

Fig. 2 Sketch of the simulation domain of the 2D planar magnetic arch plasma expansion. Only one half of the arch is simulated, taking advantage of the symmetry plane Oyz (bottom of the figure). The thruster outlet is located on the left of the domain. The rest of the boundaries are free (supersonic) outflow boundaries. The applied magnetic field $\boldsymbol{B}_a$ strength and streamlines are shown. Without loss of generality, $\boldsymbol{B}_a$ is taken to point outward in this part of the arc.

computed analytically as

$$\boldsymbol{B} = \frac{\mu_0 I}{2\pi\rho}\mathbf{1}_\theta; \qquad \psi_B = -\frac{\mu_0 I}{2\pi}\ln\rho, \tag{3}$$

where ρ, θ are polar coordinates around the wire, and $\mathbf{1}_\theta$ is the polar direction. The contribution of each wire is added to obtain the expressions for the total applied field, which is shown in figure 2. Observe that the arrangement of wires is antisymmetric about the Oyz plane.

The relevant collisionless fluid equations for electrons e and ions i are:

$$\frac{\partial n}{\partial t} + \nabla\cdot(n\boldsymbol{u}_e) = 0, \tag{4}$$

$$0 = -\nabla(nT_e) + n\nabla\phi - n\boldsymbol{u}_e \times \boldsymbol{B}, \tag{5}$$

$$\frac{\partial n}{\partial t} + \nabla\cdot(n\boldsymbol{u}_i) = 0, \tag{6}$$

$$\frac{\partial n\boldsymbol{u}_i}{\partial t} + \nabla\cdot(n\boldsymbol{u}_i\boldsymbol{u}_i) = -n\nabla\phi + n\boldsymbol{u}_i \times \boldsymbol{B}. \tag{7}$$

These equations have been complemented with the quasineutrality condition

$$n \equiv n_e = n_i. \tag{8}$$

From equation (5), we infer that, since there are no pressure gradients nor electric fields in the uniform $\mathbf{1}_y$ direction, there is no electron fluid velocity along $\mathbf{1}_\perp$. Therefore we write the electron fluid velocity as:

$$\boldsymbol{u}_e = u_{ye}\mathbf{1}_y + u_{\parallel e}\mathbf{1}_b. \tag{9}$$

Furthermore, the electrons are assumed polytropic with the simple law $T_e = n^{\gamma-1}$. We note that:

$$\frac{1}{n}\nabla(nT_e) = \frac{1}{n}\nabla n^\gamma = \gamma n^{\gamma-2}\nabla n = \gamma T_e \nabla\ln n = \frac{\gamma}{\gamma-1}\nabla n^{\gamma-1},$$

where the last equality holds for $\gamma \neq 1$. Observe that the relevant dimensionless sound speed is $c_s = \sqrt{\gamma}$, so the in-plane ion speed $\tilde{u}_i = \sqrt{u_{zi}^2 + u_{xi}^2}$ is roughly equivalent to the ion Mach number M_i, the only difference being a factor of $\sqrt{\gamma}$, i.e., $M_i = \tilde{u}_i/\sqrt{\gamma}$.

With these premises, equation (5) becomes

$$0 = -\nabla \left[\frac{\gamma}{\gamma - 1}(n^{\gamma-1} - 1) - \phi \right] - u_{ye} B \mathbf{1}_\perp. \tag{10}$$

We find that the electron energy H_e is conserved along magnetic lines,

$$H_e(\psi_B) = \frac{\gamma}{\gamma - 1}(n^{\gamma-1} - 1) - \phi, \tag{11}$$

and that the u_{ye} velocity can be computed from the map of ∇H_e:

$$u_{ye}(\psi_B) = -\frac{1}{B}\frac{\partial H_e}{\partial \mathbf{1}_\perp} = -\frac{\mathrm{d}H_e}{\mathrm{d}\psi_B}. \tag{12}$$

This u_{ye} contains the sum of the diamagnetic and $\boldsymbol{E} \times \boldsymbol{B}$ drifts, which are the only 1st-order drifts in the problem (and indeed, they scale as $1/B$). The function H_e, its derivative $\mathrm{d}H_e/\mathrm{d}\psi_B$, and u_{ye} are computed from the boundary conditions at $z = 0$ on each magnetic line a priori, i.e. before solving the rest of the problem. Observe that only one value of H_e may be imposed per magnetic line, and this restricts the set of valid boundary conditions elsewhere.

Lastly, we note that $u_{\parallel e}$ does not appear in equations (5)–(7), and is effectively uncoupled from the rest of the problem, Indeed, it can be computed from equation (4) and the boundary conditions a posteriori, after all other variableshave been solved for. In the steady state, this equation reduces to

$$\frac{\partial n u_{\parallel e}/B}{\partial \mathbf{1}_b} = 0. \tag{13}$$

Observe that, in steady state, the closed magnetic line system of the MAT forbids any electrons from the collisionless plasma to leave the domain since $u_{\perp e} = 0$, and therefore we must have $u_{\parallel e} = 0$ everywhere, and no electrons can be emitted from the thruster. This sets an additional consistency requirement on the boundary conditions, which must set $u_{\parallel e} = 0$ there. This conclusion is understood as one of the limitations of the collisionless and $\beta = 0$ model presented here, and one that will change drastically whenever one or the other (or both) assumptions are lifted. This aspect of the model is discussed in more detail in section IV.

The electron equations have therefore been reduced to (1) a conservation law for H_e, and (2) an algebraic expression for u_{ye}. Equation (11) may then be regarded as the law that provides the electrostatic potential on each magnetic line as a function of the electron density and the magnetic streamline function:

$$\phi(n, \psi_B) = \frac{\gamma}{\gamma - 1}[n^{\gamma-1} - 1] - H_e(\psi_B). \tag{14}$$

Introducing this relation into the ion momentum equation (7) to eliminate ϕ and using (12) to eliminate u_{ye} results in:

$$\frac{\partial n}{\partial t} + \frac{\partial n u_{zi}}{\partial z} + \frac{\partial n u_{xi}}{\partial x} = 0 \tag{15}$$

$$\frac{\partial n u_{zi}}{\partial t} + \frac{\partial n u_{zi} u_{zi}}{\partial z} + \frac{\partial n u_{xi} u_{zi}}{\partial x} + \frac{\partial n^\gamma}{\partial z} = -n \left(\frac{\partial H_e}{\partial \psi_B} + u_{yi} \right) B_x, \tag{16}$$

$$\frac{\partial n u_{xi}}{\partial t} + \frac{\partial n u_{xi} u_{zi}}{\partial z} + \frac{\partial n u_{xi} u_{xi}}{\partial x} + \frac{\partial n^\gamma}{\partial x} = n \left(\frac{\partial H_e}{\partial \psi_B} + u_{yi} \right) B_z, \tag{17}$$

$$\frac{\partial n u_{yi}}{\partial t} + \frac{\partial n u_{yi} u_{zi}}{\partial z} + \frac{\partial n u_{xi} u_{yi}}{\partial x} = n(u_{zi} B_x - u_{xi} B_z), \tag{18}$$

and the map of ϕ can be computed a posteriori from equation (14).

In the steady state, each species admits a streamfunction ψ_j such that $\nabla\psi_j = -n u_{xj} \mathbf{1}_z + n u_{zj} \mathbf{1}_x$, for $j = e, i$. Additionally, the last ion equation (18) can be integrated to yield (see [5] for the analogous equation in the axisymmetric MN):

$$u_{yi} + \psi_B = D(\psi_i), \tag{19}$$

where $D(\psi_i)$ is a function of the ion streamfunction that can be determined from the boundary conditions at the thruster outlet.

When the dimensionless $B_{a0} \equiv \Omega_{i0} \sim O(1)$ or less (which is the case of interest for the first MAT prototype), ion magnetization is weak, and the last term in the ion momentum equations (ion magnetic force) is typically small. Then, if $u_{yi} \ll 1$ initially, it remains so everywhere else, so $u_{yi}B \ll 1$ and the electron magnetic force dominates in the right hand side of equations (16) and (17).

The ion equations (15)–(18) must be integrated with boundary conditions for $n, \boldsymbol{u}_i$. The boundary conditions at the thruster outlet must be specified in each simulation case, and for the present work, they are presented in section III. At the plane of symmetry $x = 0$ the condition $u_{xi} = 0$ is imposed, while all other boundaries allow the free (supersonic) outflow of ions. As initial conditions, any gross approximation to the expected steady state flow can be used to speed up the convergence.

A. Numerical integration

The differential equations (15)–(17) are in conservative form, and can be formally written as

$$\frac{\partial \boldsymbol{Q}}{\partial t} + \nabla \cdot \mathbf{F} = \boldsymbol{R}. \tag{20}$$

where

$$\boldsymbol{Q} = \begin{bmatrix} n \\ nu_{zi} \\ nu_{xi} \\ nu_{yi} \end{bmatrix}; \qquad \mathbf{F} = \begin{bmatrix} nu_{zi} & nu_{xi} \\ nu_{zi}^2 + n^\gamma & nu_{zi}u_{xi} \\ nu_{zi}u_{xi} & nu_{xi}^2 + n^\gamma \\ nu_{zi}u_{yi} & nu_{xi}u_{yi} \end{bmatrix}; \qquad \boldsymbol{R} = \begin{bmatrix} 0 \\ -n\left(\partial H_e/\partial\psi_B + u_{yi}\right)B_x \\ n\left(\partial H_e/\partial\psi_B + u_{yi}\right)B_z \\ n(u_{zi}B_x - u_{xi}B_z) \end{bmatrix}. \tag{21}$$

The equations are discretized using a discontinuous Galerkin (DG) method, which for zeroth-order polynomials coincides with the finite volume method for all purposes. The DG approach enables improving the solution by refining the mesh size and by increasing the order of the approximation. After multiplying equation (20) by a test vector $\boldsymbol{V}$, integrating in an element $D_l = k$ with boundary ∂D_k, and using integration by parts, the following weak form is obtained:

$$\int_{D_k} \boldsymbol{V} \cdot \frac{\partial \boldsymbol{Q}}{\partial t} \mathrm{d}\Omega + \int_{\partial D_k} \boldsymbol{V} \cdot \mathbf{F} \cdot \mathrm{d}\boldsymbol{S} - \int_{D_k} \mathbf{F} : \nabla \boldsymbol{V} \mathrm{d}\Omega = \int_{D_k} \boldsymbol{V} \cdot \boldsymbol{R} \mathrm{d}\Omega, \tag{22}$$

where $\mathrm{d}\Omega$ is the area differential and $\mathrm{d}\boldsymbol{S}$ is the outward-oriented area vector differential. Upon summation over all elements of the domain, the second integral must be substituted by the corresponding numerical flux integral on all internal boundaries, taking into account the jump conditions across neighboring elements:

$$\int_{\Gamma_{int}} \boldsymbol{V} \cdot \mathbf{F} \cdot \mathrm{d}\boldsymbol{S} = \int_{\Gamma_{int}} (\boldsymbol{V}^+ - \boldsymbol{V}^-) \cdot \mathbf{H} \mathrm{d}\boldsymbol{S} \tag{23}$$

where Γ_{int} are the internal facets of the discretization, symbols '+' and '−' indicate the values of a discontinuous variable on one side and the other side of an internal facet, with $\mathrm{d}\boldsymbol{S}$ pointing toward the + side, and $\mathbf{H}$ is a numerical flux function. In this work the numerical flux function is chosen to be the so-called local Lax-Friedrichs flux given by

$$\mathbf{H} = \frac{1}{2}(\mathbf{F}(\boldsymbol{Q}^+) - \mathbf{F}(\boldsymbol{Q}^-) + \alpha(\boldsymbol{Q}^+ - \boldsymbol{Q}^-)), \tag{24}$$

with α computed as the maximum of all eigenvalues of the normal flux Jacobian evaluated in each side of the facet.

A similar treatment is done on the external boundary facets, denoted by Γ_{ext}, except that on those facets the + side corresponds to the weakly imposed boundary conditions. The external boundary is further decomposed into Γ_{in}, Γ_{out}, and Γ_{wall} for supersonic inflow, supersonic outflow and wall/symmetry plane boundaries respectively. At the inflow boundary, the $\boldsymbol{Q}^+$ vector on the + side is fully determined by the desired inflow conditions. At the supersonic outflow boundary, the $\boldsymbol{Q}^+$ vector is taken equal to $\boldsymbol{Q}^-$ (i.e., the value of $\boldsymbol{Q}$ on the corresponding boundary element of the domain, and finally, at wall/symmetry plane conditions the $\boldsymbol{Q}^+$ vector equals $\boldsymbol{Q}^-$ in the density and parallel flux, but imposes zero perpendicular flux.

The discretized problem is initially integrated in time using a third order Strong Stability Preserving Runge-Kutta scheme given by [24] to prepare initial conditions for the steady-state solver. After a sufficient amount of time steps, the

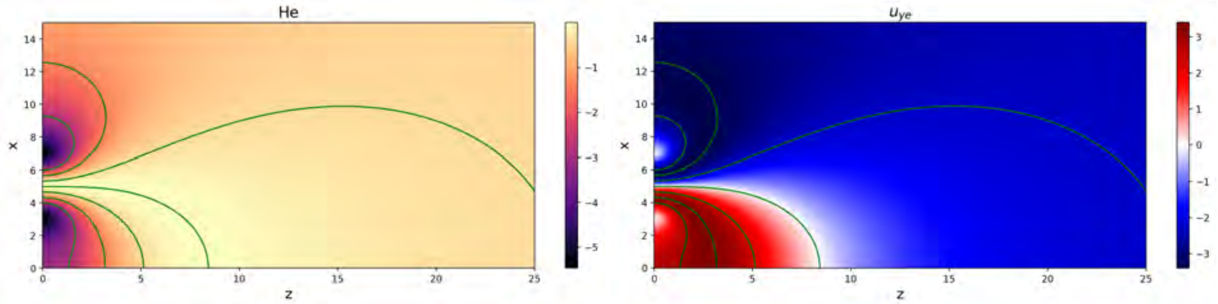

Fig. 3 Electron energy function H_e and electron out-of-plane velocity u_{ye} which result from the applied magnetic field and the upstream plasma conditions. Magnetic lines of the applied field B_a are included in the plots for reference.

steady state version of the equation is solved for. The numerical implementation of the model employs GMSH[25] and FENICS[26] as open-source building blocks. The code has been verified successfully by simulating simple cases: (1) plasma flowing in a straight, uniform magnetic field (2) 2D planar MN, and comparison against the existing DIMAGNO code [5]. Mass and momentum are successfully conserved in the simulation. A convergence study with mesh size and polynomial order was also conducted and confirmed the correct behavior of the code.

III. Simulation results

The ion beam boundary conditions at the outlet of the thruster ($z = 0$) are modeled as follows:

$$n(x) = 10^{-3(x-5)^2}; \qquad u_{zi}(x) = 1.2; \qquad u_{xi}(x) = 0; \qquad u_{yi}(x) = 0; \qquad \phi(x) = 0; \tag{25}$$

i.e., the plasma density profile is assumed Gaussian, centered on $x = 5$ falling to $n = 10^{-3}$ on $x = 4$ and $x = 6$ There is an initial x-equilibrium between the electron pressure and the magnetic force, with null electric field in the x direction. Importantly, we extend the Gaussian profile all the way from $x = 3$ to $x = 7$, where the thin wires that generate the magnetic field are located, to prevent regions with strictly zero plasma density, which would otherwise misbehave with the current numerical implementation. The value of the polytropic index of electrons is set to $\gamma = 1.2$. Thus, the initial value of u_{zi} corresponds with an ion Mach number of $M_i = 1.095$. The value of B_{a0}, which also describes the ion magnetization degree, is $B_{a0} = 1$ (low-mild ion magnetization).

These conditions completely fix the value of H_e at the thruster outlet and neighboring space, and therefore on the magnetic lines that span the whole the domain. The map of H_e plays a crucial role in the plasma response as its gradient ∇H_e drives the electron magnetic force, and is part of discussion in section IV. The resulting profile of H_e and the u_{ye} that follows are plotted in figure 3. As it can be observed, the gradient of H_e causes the electron out-of-plane velocity u_{ye} to be positive and negative below and above the magnetic centerline of the plasma outlet, respectively, resulting in a magnetic force that confines the electron pressure to the corresponding magnetic tube. Accordingly, electrons in the inner part of the arch (in red in the right panel of figure 3) always experience a radially-outward magnetic force (i.e., positive thrust), while those electrons on the outer part of the arch (in blue in the figure) experience a radially-outward force only in the first part of the expansion, where $B_x > 0$, and a radially-inward magnetic force in the later part of the expansion, where $B_x < 0$.

A uniform unstructured mesh with cell diameter $h = 0.29$ and order $p = 1$ polynomials are used to solve the plasma expansion. Figure 4 displays the steady-state solutions for the plasma density n, electron temperature T_e, electrostatic potential ϕ, and in-plane ion Mach number M_i with the ion streamlines. Several aspects of these results stand out. (1) similarly to a MN, the plasma expansion is initially guided by the magnetic field, but as the (essentially unmagnetized) ions accelerate, their streamlines do not adhere to the magnetic lines, separating inward as in the axisymmetric MN case [6]. The plasma density, electron temperature, and electrostatic potential all decrease axially. (2) an oblique shock structure originates where the ion streamlines from the two thruster outlets approach the symmetry plane. Ion fluid streamlines are deflected, and plasma density, electron temperature, and electrostatic potential rise after the shock, while ion velocity decreases accordingly. (3) Ion Mach number increases along the expansion and falls through the shock, but ions remain supersonic. There is a small fraction of ion current expanding outward along the wings of the jet exiting the thruster. Our verification tests show that the numerical diffusion of the scheme affects the amount of plasma in

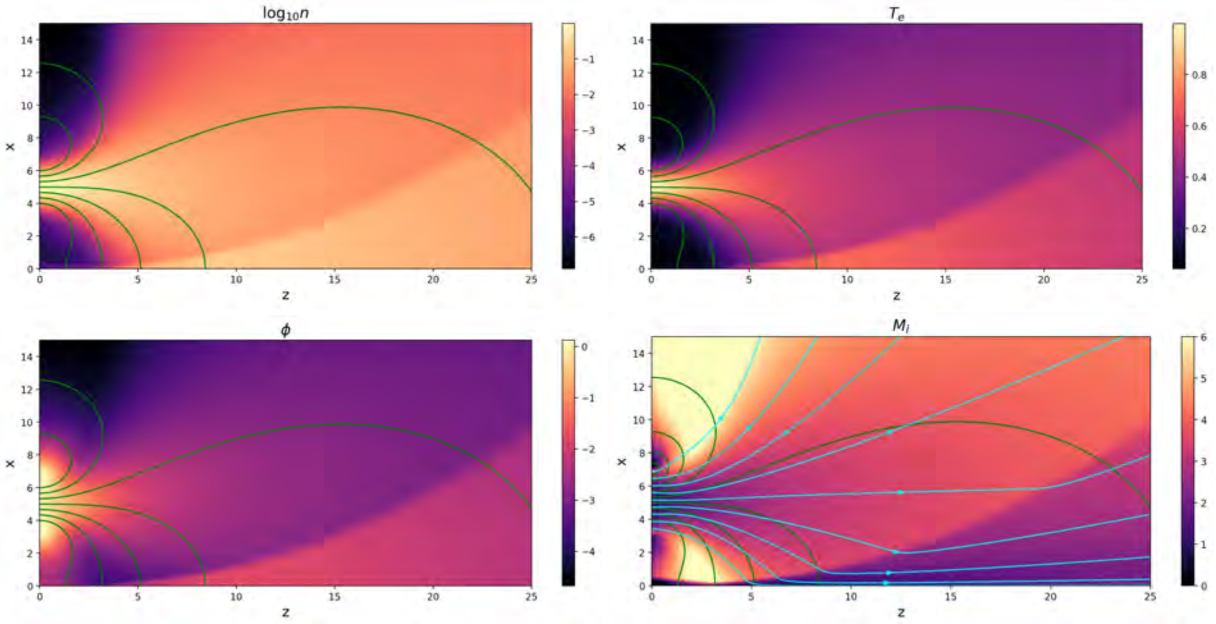

Fig. 4 Plasma density n, electron temperature T_e, electrostatic potential ϕ, and in-plane ion Mach number M_i with the ion streamlines. Background magnetic lines of the applied field are included in the plots for reference.

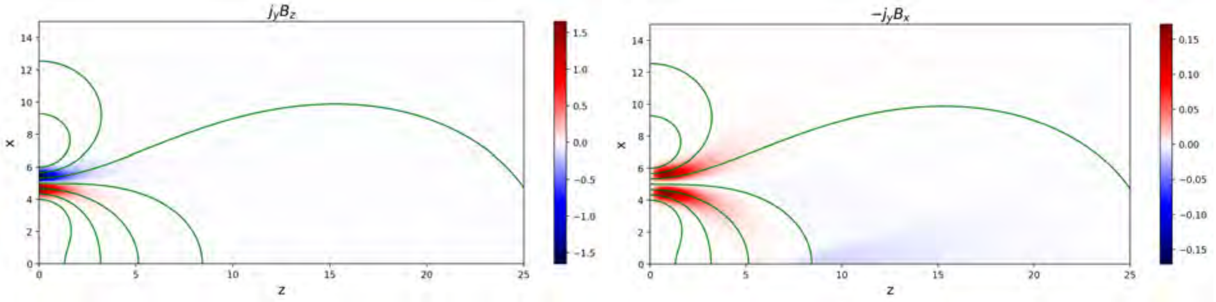

Fig. 5 Magnetic force density in the axial ($-j_y B_x$) and radial ($j_y B_z$) directions.

this region, but does not alter the essence of the conclusions reported here. (4) The ions are not confined to the closed magnetic tube that connects the two thruster outlets, but are able to form a jet that propagates beyond it to infinity. This last observation is crucial to the validity of the magnetic arch concept and for the operation of a cluster of two cylindrical EPTs with opposing magnetic polarities.

The x and z magnetic force densities $j_y B_z$ and $-j_y B_x$ respectively, where $j_y = n(u_{yi} - u_{ye})$ is the plasma current density in the out of plane direction, are depicted in figure 5. We note that j_y is dominated by the electron contribution everywhere in the domain for the current magnetization level ($B_{a0} = 1$), i.e., the ion contribution is negligible, and that the product $j_{ye} B_a$ is essentially independent of the magnitude B_{a0}. The force densities are largest near the thruster exit. The x force density, essentially perpendicular to the magnetic lines at the beginning of the expansion, confines the plasma expansion laterally and limits the divergence of the jet. The z force density gives rise to magnetic thrust, and is seen to be large and positive at the beginning of the expansion, where n, T_e and B_a are large. A small negative contribution exists downstream where the lines of $\boldsymbol{B}_a$ curve back toward the other thruster exit as expected. This negative contribution is most noticeable in the region after the shock wave, where plasma density (and therefore the out-of-plane current) increases locally again. These characteristics are consequential on the magnetic force density and the generation of magnetic thrust: while positive thrust is generated initially, in the region where the magnetic lines of each thruster exit connect the magnetic force generates drag, lowering the net thrust of the device.

As follows from the sum of the electron and ion momentum equations (5) and (7), the magnetic thrust force generated

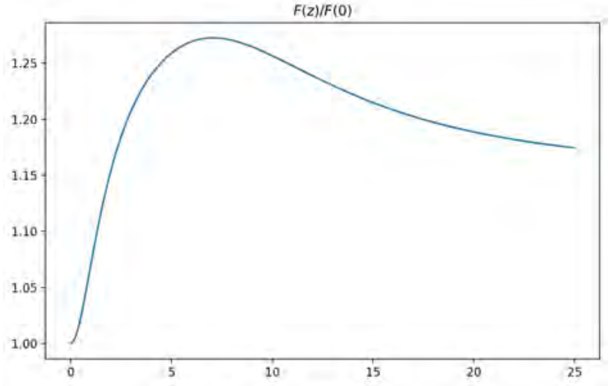

Fig. 6 Thrust integral over z-const surfaces, as a function of z. Values have been normalized with the total momentum flux at the thruster exit.

in a control volume can be computed equivalently as:

$$F(z) - F(0) = \int_{\Omega(z)} -j_y B_x \mathrm{d}\Omega = \int_{\partial\Omega(z)} [(nu_{zi}^2 + n^\gamma)\mathbf{1}_z + nu_{xi}u_{zi}\mathbf{1}_x] \cdot d\boldsymbol{S} \tag{26}$$

Where $\Omega(z)$ is a rectangular control volume that spans the domain from the initial plane $z = 0$ to a variable axial position z, and $\partial\Omega(z)$ is its boundary.

Figure 6 displays this integral force $F(z)$ in the control volume $\Omega(z)$, normalized with $F(0)$, the initial momentum flux of the plasma leaving the thruster outlets. Positive magnetic thrust is produced initially, in the first part of the expansion. When the plasma approaches the bend in the magnetic lines and the shock, a minor contribution of negative thrust (i.e. magnetic drag) results, and $F(z)$ decreases by a small amount. As indicated above, this is a natural consequence of the closed shape of the magnetic lines and the maps of n, u_{ye}, which give rise to the negative axial magnetic force density shown in figure 5.

This drop in the produced thrust is expected to change when the plasma-induced magnetic field $\boldsymbol{B}_p$ is included in the simulation, as it would stretch the magnetic lines downstream and change the topology of the field as a result.

A. Plasma-induced magnetic field

The in-plane plasma-induced magnetic field $\boldsymbol{B}_p$ has its own streamfunction ψ_{Bp}. Ampère's equation for ψ_{Bp} reduces to a manifestly elliptic partial differential equation:

$$\frac{\partial B_{px}}{\partial z} - \frac{\partial B_{pz}}{\partial x} = -\frac{\partial^2 \psi_{Bp}}{\partial z^2} - \frac{\partial^2 \psi_{Bp}}{\partial x^2} = \mu_0 j_y = \beta_0 B_{a0}^2 j_y, \tag{27}$$

where $\beta_0 = \mu_0 / B_{a0}^2$ is the β parameter at the centerpoint of the thruster outlet, already-normalized with n_0 and T_{e0}. Clearly, the plasma-induced magnetic field is zero in the $\beta_0 = 0$ limit, but we can estimate the $\boldsymbol{B}_p$ that would result for different values of β, using the j_y obtained from the $\beta_0 = 0$ simulation. Since $j_y B_a$ is essentially independent of B_{a0} in the low ion magnetization regime under consideration, the group $B_p/(\beta_0 B_{a0})$ is also essentially independent of β_0 and B_{a0}. Of course, for $\beta \neq 0$, the plasma and $\boldsymbol{B}_p$ solutions are coupled, and ought to be determined together, self-consistently, a task that is not afforded here.

Figure 7 displays the estimated $\boldsymbol{B}_p$ field using standard continuous finite elements to solve the elliptic equation (27), with $B_{pz} = 0$ boundary conditions on the symmetry plane. At present, in the rest of the boundary $B_{px} = 0$ is arbitrarily imposed. Clearly, these boundary conditions (and also the fact that we are ignoring the j_y currents outside of the simulated domain) have an effect on the resulting $\boldsymbol{B}_p$. To partially mitigate this, the peripheral part of the domain has been cut off from this figure and the following one (figure 8). Future work must assess the extent of the boundary effects and improve the computation of $\boldsymbol{B}_p$ with either larger domains or adequate matching layers at the boundaries.

Figure 8 displays the would-be total magnetic field $\boldsymbol{B} = \boldsymbol{B}_a + \boldsymbol{B}_p$ for different values of β_0 and the streamlines for $\psi_B = \psi_{Ba} + \psi_{Bp}$. As β_0 is increased from 0, $\boldsymbol{B}_p$ stretches the field lines downstream and lowers the total field magnitude at the symmetry plane. A separatrix forms downstream, visible inside the retained domain already at $\beta_0 = 0.05$, and the

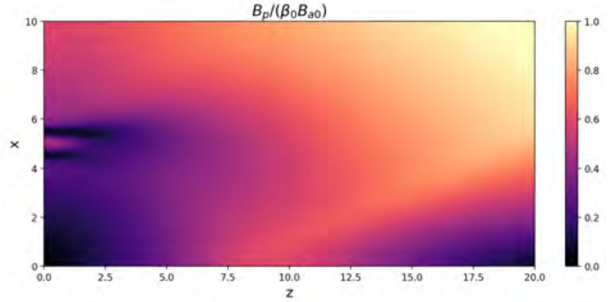

Fig. 7 Induced magnetic field strength derived from the out-of-plane plasma current j_y.

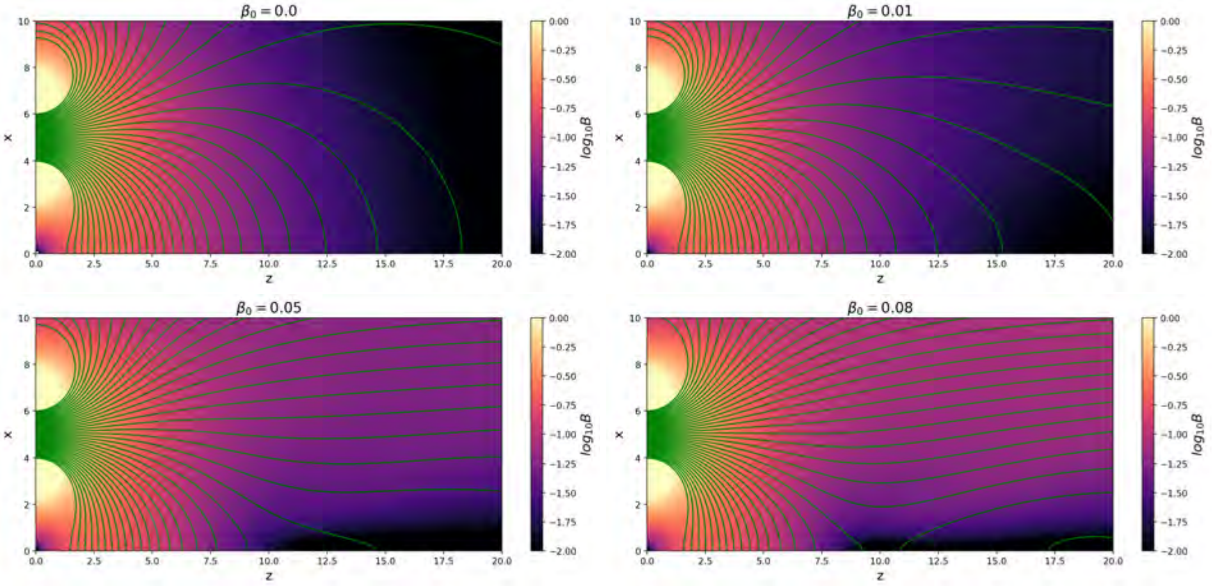

Fig. 8 Total magnetic field $\boldsymbol{B} = \boldsymbol{B}_a + \boldsymbol{B}_p$ strength and streamlines for different values of β_0, as indicated above the plots.

topology of the the magnetic arch changes drastically: (1) on the one hand, the innermost lines continue to connect with the symmetry plane and therefore with the other exit of the thruster. Electrons in this region continue to be magnetically trapped under the assumptions of the model. (2) On the other hand, the outermost part of the field now connects to infinity, and electrons there can expand freely, their parallel motion only restricted by the electrostatic field as in an axisymmetric MN. These lines are now capable of carrying a neutralizing electron current. (3) Beyond the separatrix, a third region forms whose magnetic lines are disconnected from the plasma source. Electrons in these region must arrive during the transient set-up of the plume, due to collisional effects, or due to demagnetization near the X point in the field.

These results suggest that the plasma-induced field $\boldsymbol{B}_p$ plays a central role in shaping the expansion and determining the electron properties in the plume, including their current.

IV. Discussion

The results of the previous section merit additional discussion. The following points are examined in particular. Firstly, it is observed that our plasma solution in the collisionless, $\beta_0 = 0$ case has two outstanding singular characteristics that are not expected outside of this limit: (i) The fully-magnetized, collisionless electrons have zero perpendicular velocity; while the steady-state electron continuity equation is satisfied, the transient version of this equation is not. (ii) Relatedly, electrons also have zero parallel velocity along the closed magnetic lines in the steady state, and therefore there is no net flow of electrons from the device. Other mechanisms (collisions, out-of-plane electric field E_y, plasma-induced field) are needed to explain the transient set-up of the plasma density in the plume, which have not been considered here. These possibilities are preliminary explored next.

The main effect of non-zero collisions can be understood by including a new term in electron momentum equation (5), which now becomes

$$0 = -\nabla(nT_e) + n\nabla\phi - n\boldsymbol{u}_e \times \boldsymbol{B} - \boldsymbol{R}_e, \tag{28}$$

where $\boldsymbol{R}_e = nm_e\nu_e\boldsymbol{u}_e$ is a simple representation of the collisional term. The y projection of this equation yields

$$u_{\perp e}B = \chi^{-1}u_{ye}, \tag{29}$$

with $\chi = B/(m_e\nu_e)$ the Hall parameter. As perpendicular flow is now allowed, electron current can be extracted from the thruster and $u_{\parallel e} \neq 0$ in general in steady state.

An electric field in the out-of-plane direction, $E_y\mathbf{1}_y$, can also enable perpendicular electron flux. The $\boldsymbol{E} \times \boldsymbol{B}$ drift induced by this field generates a collisionless $u_{\perp e}$ and therefore $u_{\parallel e} \neq 0$ in general in steady state, as in the previous point. This mechanism may play a role in 3D MAT expansions, where E_y may arise if the plasma undergoes lateral polarization, but is not present in the 2D geometry studied here.

Nevertheless, the mechanism that is likely to introduce the largest change on the plasma response is the plasma-induced magnetic field $\boldsymbol{B}_p$, as advanced already in the above. Indeed, it is expected that the plasma expansion will be qualitatively distinct in the $\beta_0 \neq 0$ cases of practical interest (even if β_0 is small), due to the topological change of the total magnetic field. While we have not demonstrated this self-consistently here, it has been shown that even for small β_0, $\boldsymbol{B}_p$ opens the closed-line geometry and stretches it to infinity, and that the plasma-induced magnetic field eventually dominates the applied one, forming a separatrix that delimits a new magnetic region downstream. This new magnetic topology does enable the extraction of an electron current along the now-open, stretched magnetic lines, even in the full-magnetization, collisionless, 2D planar limit. Interestingly, electron parallel velocity on the magnetic lines that remain closed (nearer to the device) will continue to be zero in the limit of the present model, and therefore the existence of different groups of electrons (e.g. trapped, free streaming) can already be inferred. Finally, the effect of $\boldsymbol{B}_p$ will naturally increase the plume divergence angle, as it does in a simple MN [23].

Secondly, another major aspect to be discussed is the influence of the conservation of H_e in the model. The profile of H_e that is defined at the upstream plane by the boundary conditions on n, T_e, and ϕ fully determines H_e in the rest of the domain, and therefore ∇H_e, which dictates the magnetic force density in the plume. However, while it is reasonable to prescribe H_e on the plasma-carrying magnetic lines that connect with the source, it is not evident what should be the condition on the external lines outside of this main magnetic tube. Here, in this first simulation, we have opted to define H_e there by setting $n \simeq 0$ and $\phi = 0$ at the upstream plane. But this means that as unmagnetized ions travel downstream, traversing the magnetic lines, and exit the main magnetic tube (i.e., the tube that connects with the thruster exit), they encounter a relatively large electrostatic barrier (induced by ∇H_e and the rising density on those external lines) that decelerates them, in effect lowering thrust. Future studies must analyze other H_e profiles (or equivalently, other initial ϕ profiles), and future versions of the model must explore other approaches of calculating H_e on those external lines, which likely will rely on mechanisms outside the present model. This will also affect the upcoming self-consistent simulation of the plasma response with the induced magnetic field, as values of H_e must be produced for the new magnetic region beyond the separatrix, on lines that do not connect with the upstream plane. Collisions, electron inertia, and electron kinetics can possibly afford such mechanisms, or even replace the conservation of H_e along each magnetic line with a different law. Incidentally, note that if H_e were constant everywhere (which can always be achieved with the right choice of ϕ upstream), there would be no magnetic force on the electron fluid and the magnetic guiding effect would vanish completely.

Thirdly, the applicability of the results of the two-dimensional planar model to the actual 3D MAT configuration remains to be assessed. While it is currently expected that the planar model captures the essence of the mechanisms at play in the actual device, adding bounds to the plasma in the third dimension can have some unexpected effects, such as the possible set up of a polarization E_y field that further changes the axial dynamics due to the $\boldsymbol{E} \times \boldsymbol{B}$ drift as discussed above. The 3D geometry must be eventually simulated to ascertain all this.

V. First MAT prototype

Before closing this paper, the ongoing experimental efforts of project ZARATHUSTRA are overviewed.

A prototype has been developed to prove the concept of the MAT configuration as shown in figure 9. The device features a 'C'-shaped discharge chamber, surrounded by 10 magnetic coils that generate the applied field $\boldsymbol{B}_a$, which is

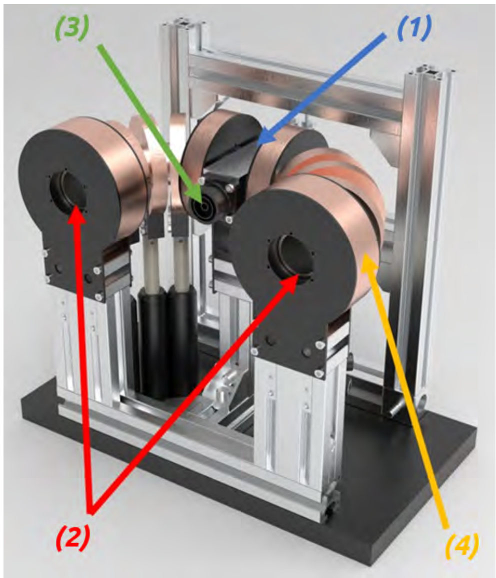

Fig. 9 3D rendering of the first prototype of the magnetic arch thruster (MAT). (1) represents the neutral gas injection on the back of the ionization chamber. (2) points out the two exhausts of the C-shaped ionization chamber. (3) designates the microwave power injection. (4) pictures the coils distributed through the C-shaped ionization chamber to enable the ECR, confine the plasma and accelerate it in the external expanding magnetic arch.

essentially parallel to the chamber walls. A neutral gas (nominally Xe) injection system is located in the rear part of ionization chamber. Microwave power at 2.45 GHz is injected from the front via a coaxial cable and a pin antenna immersed into the chamber. The magnetic field strength and the wave frequency are matched to generate a controllable electron-cyclotron resonance (ECR) surface, aimed at efficiently coupling the power to the plasma. Two coaxial to waveguide adapters are used as a DC block to enable the thruster to electrically float with respect to ground. A solid state microwave generator is used to deliver up to 1 kW of power to the thruster. The thruster general characteristics are shown in table 1.

The magnetic coils are divided into six sets, whose current can be controlled independently: the two principal coils (PC) are the ones used to produce a uniform magnetic field in the central part of the ionization chamber. The two groups of segment coils (SC) are made to curve the magnetic field in the two arms of the chamber. Finally, two magnetic nozzle coils (MN) at each exit of the device strengthen the field there and shape the external arch. The nominal, simulated magnetic field is shown in figure 10, where the position of the ECR surface has been highlighted. This resonance can be placed near the outlets of the thruster to favor plasma generation close to the exits.

Plasma chamber length	364 mm
Plasma chamber radius	29.7 mm
Microwave power	10 – 1000 W
Estimated mass flow rate (Xe)	[1 ; 100] sccm
MW frequency	2.45 GHz
B-resonance	875 G
Max electromagnet power	1500 W

Table 1 Summary of the first MAT prototype characteristics.

The assembled prototype can be seen in figure 11. First ignition tests are to follow soon to debug the configuration and then validate the proof of concept of the device.

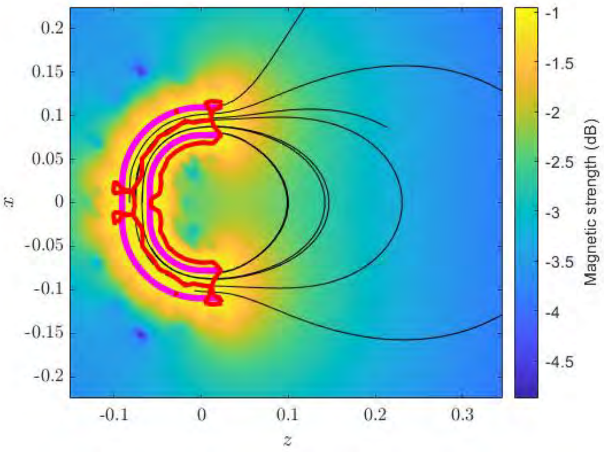

Fig. 10 **Colormap of the midsection of the 3D magnetic field of the MAT prototype. The 875 G magnitude line of the magnetic field is highlighted in red. The magenta lines correspond to the thruster walls.**

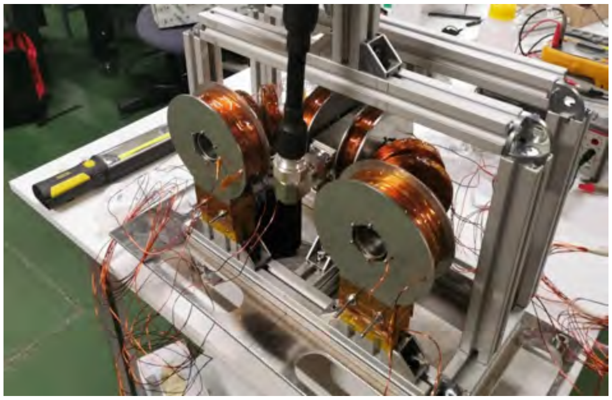

Fig. 11 **Picture of the first prototype of the magnetic arch thruster.**

VI. Conclusion and future work

A first model of the external expansion of the novel magnetic arch thruster has been presented, which already describes much of its interesting plasma physics in spite of its simplifying assumptions. The ions are seen to form a free jet that traverses the closed lines of the magnetic field, even if electrons are fully magnetized. A shock-like structure forms when the two beams coming out of the thruster exits interact. A net positive magnetic thrust is produced, and it is observed that most of the positive contribution comes from the initial stages of the expansion, while a small negative (drag) component results from the region where the magnetic lines bend back to the device. This coincides with expectation, and it has been hypothesized and illustrated with computations that the plasma-induced magnetic field will change the total field topology, resulting in a different expansion. The magnetic arch topology is also relevant to clusters of traditional, cylindrical EPTs. Enhancements to the model have been evaluated and discussed, and future work must add self-consistently the plasma-induced magnetic field, 3D effects, and collisions. Finally, the first prototype of the MAT, being developed in parallel, has been showcased and described.

Acknowledgments

The ZARATHUSTRA project has received funding from the European Research Council (ERC) under the European Union's Horizon 2020 research and innovation programme (grant agreement No 950466)

References

[1] Ahedo, E., "Plasmas for space propulsion," *Plasma Physics and Controlled Fusion*, Vol. 53, No. 12, 2011, p. 124037. URL `http://stacks.iop.org/0741-3335/53/i=12/a=124037`.

[2] Mazouffre, S., "Electric propulsion for satellites and spacecraft: established technologies and novel approaches," *Plasma Sources Science and Technology*, Vol. 25, No. 3, 2016, p. 033002.

[3] Bathgate, S., Bilek, M., and Mckenzie, D., "Electrodeless plasma thrusters for spacecraft: a review," *Plasma Science and Technology*, Vol. 19, No. 8, 2017, p. 083001.

[4] Takahashi, K., "Helicon-type radiofrequency plasma thrusters and magnetic plasma nozzles," *Reviews of Modern Plasma Physics*, Vol. 3, 2019, p. 3.

[5] Ahedo, E., and Merino, M., "Two-dimensional supersonic plasma acceleration in a magnetic nozzle," *Physics of Plasmas*, Vol. 17, No. 7, 2010, p. 073501.

[6] Merino, M., and Ahedo, E., "Plasma detachment in a propulsive magnetic nozzle via ion demagnetization," *Plasma Sources Science and Technology*, Vol. 23, No. 3, 2014, p. 032001. https://doi.org/10.1088/0963-0252/23/3/032001.

[7] Merino, M., and Ahedo, E., "Magnetic Nozzles for Space Plasma Thrusters," *Encyclopedia of Plasma Technology*, Vol. 2, edited by J. L. Shohet, Taylor and Francis, 2016, pp. 1329–1351.

[8] Little, J. M., and Choueiri, E. Y., "Electron Demagnetization in a Magnetically Expanding Plasma," *Physical review letters*, Vol. 123, No. 14, 2019, p. 145001.

[9] Merino, M., Nuez, J., and Ahedo, E., "Fluid-kinetic model of a propulsive magnetic nozzle," *Plasma Sources Science and Technology*, Vol. 30, No. 11, 2021, p. 115006. https://doi.org/10.1088/1361-6595/ac2a0b, URL https://doi.org/10.1088/1361-6595/ac2a0b.

[10] Batishchev, O., "Mini-Helicon Plasma Thruster Characterization," *44th Joint Propulsion Conference, Hartford, CT*, 2008.

[11] Pavarin, D., Ferri, F., Manente, M., Curreli, D., Guclu, Y., Melazzi, D., Rondini, D., Suman, S., Carlsson, J., Bramanti, C., Ahedo, E., Lancellotti, V., Katsonis, K., and Markelov, G., "Design of 50W Helicon Plasma Thruster," *31th International Electric Propulsion Conference*, 2009.

[12] Takahashi, K., Charles, C., and Boswell, R., "Approaching the theoretical limit of diamagnetic-induced momentum in a rapidly diverging magnetic nozzle," *Physical review letters*, Vol. 110, No. 19, 2013, p. 195003.

[13] Navarro-Cavallé, J., Wijnen, M., Fajardo, P., and Ahedo, E., "Experimental characterization of a 1 kW helicon plasma thruster," *Vacuum*, Vol. 149, 2018, pp. 69–73.

[14] Tian, B., Merino, M., and Ahedo, E., "Two-dimensional plasma-wave interaction in an helicon plasma thruster with magnetic nozzle," *Plasma Sources Science and Technology*, Vol. 27, No. 11, 2018, p. 114003.

[15] Zhou, J., Jiménez, P., Merino, M., Fajardo, P., and Ahedo, E., "Numerical Simulations of the Plasma Discharge in a Helicon Plasma Thruster," 36^{th} *International Electric Propulsion Conference*, Electric Rocket Propulsion Society, Vienna, Austria, 2019.

[16] Jiménez, P., Merino, M., and Ahedo, E., "Wave propagation and absorption in a Helicon plasma thruster source and its plume," *Plasma Sources Science and Technology*, Vol. 31, No. 4, 2022, p. 045009. https://doi.org/10.1088/1361-6595/ac5ecd, URL https://doi.org/10.1088/1361-6595/ac5ecd.

[17] Sercel, J., "Electron-cyclotron-resonance (ECR) plasma thruster research," *24th Joint Propulsion Conference*, 1988, p. 2916.

[18] Vialis, T., Jarrige, J., Aanesland, A., and Packan, D., "Direct thrust measurement of an electron cyclotron resonance plasma thruster," *Journal of Propulsion and Power*, Vol. 34, No. 5, 2018, pp. 1323–1333.

[19] Correyero, S., Merino, M., Elias, P.-Q., Jarrige, J., Packan, D., and Ahedo, E., "Characterization of diamagnetism inside an ECR thruster with a diamagnetic loop," *Physics of Plasmas*, Vol. 26, No. 5, 2019, p. 053511. https://doi.org/10.1063/1.5093980.

[20] Sánchez-Villar, A., Merino, M., and Ahedo, E., "A numerical parametric investigation on the optimal design and operation of coaxial ECR thrusters," *Space Propulsion Conference 2021*, Association Aéronautique et Astronautique de France, March 17-19, 2021.

[21] Merino, M., and Ahedo, E., "Contactless steering of a plasma jet with a 3D magnetic nozzle," *Plasma Sources Science and Technology*, Vol. 26, No. 9, 2017, p. 095001. https://doi.org/10.1088/1361-6595/aa8061.

[22] Longmier, B. W., Squire, J. P., Carter, M. D., Cassady, L. D., Glover, T. W., Chancery, W. J., Olsen, C. S., Ilin, A. V., Mccaskill, G. E., and Chang Díaz, F. R., "Ambipolar Ion Acceleration in the Expanding Magnetic Nozzle of the VASIMR ® VX-200i," *45th AIAA/ASME/SAE/ASEE Joint Propulsion Conference & Exhibit*, 2009, pp. 1–10.

[23] Merino, M., and Ahedo, E., "Effect of the plasma-induced magnetic field on a magnetic nozzle," *Plasma Sources Science and Technology*, Vol. 25, No. 4, 2016, p. 045012. https://doi.org/10.1088/0963-0252/25/4/045012.

[24] Cockburn, B., and Shu, C.-W., "The Runge–Kutta discontinuous Galerkin method for conservation laws V: multidimensional systems," *Journal of Computational Physics*, Vol. 141, No. 2, 1998, pp. 199–224.

[25] Geuzaine, C., and Remacle, J.-F., "Gmsh: A 3-D finite element mesh generator with built-in pre-and post-processing facilities," *International journal for numerical methods in engineering*, Vol. 79, No. 11, 2009, pp. 1309–1331.

[26] Logg, A., Mardal, K.-A., and Wells, G., *Automated solution of differential equations by the finite element method: The FEniCS book*, Vol. 84, Springer Science & Business Media, 2012.